

Magnetic frustration and weak Mn magnetic ordering in EuMn_2P_2

Sarah Krebber,^{1,*} Jörg Sichelschmidt,² Pierre Chailloleau,² Asmaa El Mard,¹ Marvin Kopp,¹ Michael Baenitz,² Kurt Kummer,³ Denis V. Vyalikh,^{4,5} Jens Müller,¹ Cornelius Krellner,¹ and Kristin Kliemt^{1,†}

¹*Physikalisches Institut, Goethe Universität Frankfurt am Main,
Max-von-Laue Straße 1, 60438 Frankfurt, Deutschland*

²*Max-Planck-Institut für Chemische Physik fester Stoffe, 01187 Dresden, Deutschland*

³*European Synchrotron Radiation Facility, 38043 Grenoble, France*

⁴*Donostia International Physics Center (DIPC), 20018 Donostia-San Sebastian, Spain*

⁵*IKERBASQUE, Basque Foundation for Science, 48013 Bilbao, Spain*

(Dated: January 3, 2025)

We report on the electron spin resonance (ESR), heat capacity, magnetization, nuclear magnetic resonance (NMR), magnetic circular and linear dichroism (XMCD, XMLD), as well as the electrical resistivity of EuMn_2P_2 single crystals. Antiferromagnetic order of Eu was observed in several quantities at $T_N^{\text{Eu}} = 18$ K. The temperature dependencies of ESR linewidth and resonance shift show, when approaching the Eu-ordered state, a divergence towards T_N^{Eu} , indicating the growing importance of magnetic correlations and the build-up of internal magnetic fields. An additional temperature scale of ≈ 47 K has considerable impact on linewidth, resonance field and intensity. This points to the presence of weak Mn-based ordering. The observed ESR line is interpreted as an Eu^{2+} resonance, which probes the weak magnetic background of the Mn subsystem. Such picture is suggested by the lineshape which keeps to be Lorentzian across the 47 K scale and by the ESR intensity which can be described by the same Curie-Weiss temperature above and below 47 K. In the same temperature range anomalies were observed at 48.5 K and 51 K in the heat capacity data as well as a pronounced broadening of the NMR signal of the EuMn_2P_2 samples. In XMCD and XMLD measurements, this weak magnetic order could not be detected in the same temperature range which might be due to the small magnetic moment, with a potential c -component or frustration.

I. INTRODUCTION

In recent times, trigonal antiferromagnetic materials of the EuT_2Pn_2 family ($T = \text{Cd}, \text{Zn}$; $\text{Pn} = \text{P}, \text{As}, \text{Sb}$) have become the subject of considerable research interest, as they offer the potential to investigate a range of fascinating physical phenomena including Weyl semimetal states [1–3], unusual transport properties such as colossal magnetoresistance [4–10], unconventional anomalous Hall effect [11, 12] or thermoelectric effects [13, 14]. It has recently been demonstrated that the magnetic order of the Eu^{2+} ions can be altered from AFM to FM in certain instances by means of pressure [15] or alternative preparation methods [16–18].

The related compound EuMn_2P_2 belongs to the same Eu-based 122-systems with the trigonal CaAl_2Si_2 crystal structure (space group $P\bar{3}m1$ (164)), Fig. 1. The Eu moment of this compound is located on triangular layers of Eu^{2+} with edge-shared EuP_6 octahedra, separated by low-carrier density Mn_2P_2 blocks. Neutron diffraction on EuMn_2P_2 revealed A-type AFM Eu order below 16.5 K with the moments lying in the $a - a$ plane with FM coupling in the plane and AFM coupling along the c direction

[19]. In this neutron diffraction study, no magnetic order of Mn in EuMn_2P_2 was observed [19]. This finding was further corroborated in a recent study by heat capacity and susceptibility measurements [20]. The authors of this study concluded that the long-range Mn magnetic order is suppressed by chemical pressure. Furthermore, the development of short-range Mn magnetic correlations from $T \approx 250 - 100$ K, interpreted as a precursor to covalent bond formation, was suggested [20]. This is in contrast to the related compounds EuMn_2As_2 and EuMn_2Sb_2 where phase transitions attributed to the magnetic order of Mn were visible in the heat capacity at higher temperatures ($T_N = 135$ K, $T_N = 128$ K) [21, 22]. In trigonal or hexagonal systems, a key ingredient in preventing the onset of magnetic order is geometrical frustration [23–25].

There are a number of electron spin resonance (ESR) investigations on layered Eu-pnictide systems with *tetragonal* 122-structure whereas the ESR on Eu or Mn containing compounds with *trigonal* 122-structure are rarely reported. An example of the latter is the ESR on powder samples of $\text{EuZn}_2(\text{P}, \text{As}, \text{Sb})_2$ for which ferromagnetic fluctuations were established to dominate the linewidth broadening towards the temperature of antiferromagnetic order [26, 27].

It turns out, that the ESR of EuMn_2P_2 displays some similarities to that of the Eu-pnictide 122-systems with *tetragonal* structure, such as EuFe_2As_2 . There one observes a coupling of local Eu^{2+} spins to conduction elec-

* krebber@physik.uni-frankfurt.de

† kliemt@physik.uni-frankfurt.de

trons in the FeAs layers [28–30]. Two transitions are seen in the linewidth: a weak spin-density wave (SDW) transition feature (itinerant iron magnetism) and a divergence for T approaching T_N (Eu magnetism). All spectra consist of a single exchange-narrowed Lorentzian line, also for the ESR in $\text{EuFe}_{2-x}\text{Co}_x\text{As}_2$ [31] where the linewidth features related to Eu ordering and to the SDW transition depend on the concentration of Co.

The unusual magnetic behavior of EuMn_2P_2 encouraged us to re-investigate the material in detail in a temperature range which was less studied before using ESR, heat capacity, magnetic susceptibility, NMR, XMCD, XMLD, and resistivity measurements to elucidate the lack of magnetic Mn order with respect to magnetic frustration. Our investigations show that around 50 K a weak magnetic order of Mn sets in, which is explained in detail below.

II. EXPERIMENT

A. Crystal growth and X-ray diffraction

Single crystals of EuMn_2P_2 were grown in Sn flux. Pieces of the elements europium (99.99%, Evochem), red phosphorous (99.9999%, Chempur), manganese (99.999%, Evochem) and teardrops of tin (99.9999%, Chempur) were weighed in with a stoichiometry of 14:8:11:265 (Eu:Mn:P:Sn) under inert Ar atmosphere. The elements were then put into a graphite crucible inside an evacuated quartz ampule. The ampule was loaded into a box furnace (Thermconcept), where the mixture was first heated to 450°C and held for 5 h. This step ensured that phosphorous could slowly react with the other elements. Subsequently, the mixture was heated to 1200°C and held for 12 h. The temperature was then slowly lowered to 970°C with a rate of 2 K/h and afterwards again lowered with a higher cooling rate of 10 K/h to 800°C, where the Sn flux was removed by centrifugation. Hexagonal shaped platelet-like single crystals, Fig. 1(b), were obtained and characterized using powder X-ray diffraction (XRD), energy dispersive X-ray spectroscopy (EDX) and Laue diffraction. XRD analysis yielded lattice parameters of $a = 4.1381 \text{ \AA}$ and $c = 7.0255 \text{ \AA}$, which is consistent with literature [19, 32]. XRD data were collected at different temperatures down to 10 K, confirming that no pronounced structural change in the lattice occurs. The powder diffraction patterns were recorded on a diffractometer by Bruker (D8) with Bragg-Brentano geometry and copper K_α radiation. The temperature dependent data was collected on a diffractometer D500 (Siemens) with Bragg-Brentano geometry and copper K_α radiation. The orientation of the single crystals was determined by the Laue method using an X-ray equipment “Micro 91” (Müller) with a tungsten anode.

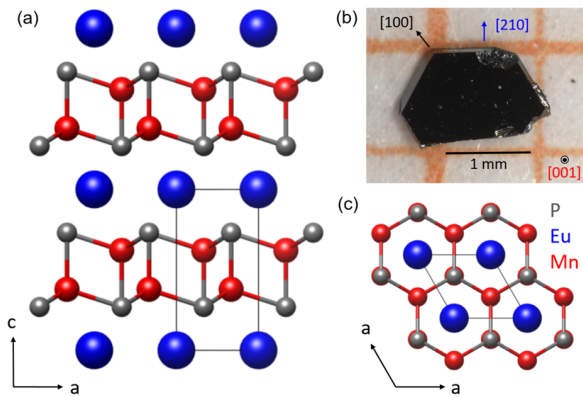


FIG. 1. (a) EuMn_2P_2 crystallizes in the CaAl_2Si_2 structure type (trigonal space group, $P\bar{3}m1$, No. 164). (b) Orientation of a single crystal of EuMn_2P_2 determined with the Laue method. The surface of the crystal is perpendicular to the c -direction. (c) View of the crystal structure along the c -direction.

B. Electron spin resonance

We carried out electron spin resonance (ESR) experiments with a standard continuous-wave spectrometer in a wide temperature range between 5 and 500 K. The ESR setup detects the power P absorbed by the sample from a magnetic microwave field ($\nu \approx 9.4 \text{ GHz}$ or 34.1 GHz) as a function of an external, transverse magnetic field H . A lock-in technique was used to improve the signal-to-noise ratio which yields the derivative of the resonance signal dP/dH . All spectra were fitted by a Lorentzian shape [33] to obtain the parameters linewidth ($\mu_0\Delta H$ being a measure of the spin relaxation), resonance field ($\mu_0 H_{\text{res}}$, as given by the resonance condition $h\nu = g\mu_B \cdot \mu_0 H_{\text{res}}$ and being determined by the g -value and internal fields), the amplitude, and the ratio of dispersion and absorption contribution D/A (being relevant for electrical conductive samples). The ESR intensity I_{ESR} is deduced from the integrated ESR spectra and is a measure of the local spin susceptibility. The spectra integration was estimated by the amplitude, linewidth, and D/A as exemplified in Ref. [34].

C. Heat capacity and magnetic measurements

Heat capacity (HC) measurements were conducted utilizing the heat capacity option of a Quantum Design Physical Property Measurement System (PPMS). The sample was affixed to a field-calibrated heat capacity puck using Apiezon N grease. In a high vacuum, the sample was subjected to a thermal pulse and its temperature response is recorded in a manner analogous to that employed in a traditional semi-adiabatic relaxation technique. To resolve weak temperature-dependent anomalies large heating pulses were used with typical temperature rises of

6 K. The data was then analyzed using the single-slope method. The magnetic susceptibility and magnetization measurements were carried out using the vibrating sample magnetometer option (VSM) of the PPMS. The crystal was fixed to the sample holder using GE varnish. The field-dependent data were collected by applying an external magnetic field up to 9 T parallel and perpendicular to the crystallographic c direction of the sample. The analysis of several samples revealed no significant deviations in the heat capacity and magnetization data.

D. Nuclear magnetic resonance

Field sweep NMR techniques were applied by use of the conventional pulsed NMR method on the ^{31}P nuclei (with nuclear spin $I = 1/2$) in the temperature range of $2\text{ K} \leq T \leq 300\text{ K}$ at fixed frequency of 40 MHz. The EuMn_2P_2 powder sample was mixed with paraffin, heated up, shook and then cured to randomize the grains. The field sweep spectra were obtained by integration over the spin echo in the time domain. Powder spectra were modelled with an anisotropic shift tensor. Shift components in the $a-a$ plane and the c direction were determined.

E. X-ray magnetic circular and linear dichroism

X-ray absorption spectroscopy measurements were conducted at the ID32 beamline of the ESRF using the high-field magnet end station [35, 36]. Samples were cleaved in UHV at low temperature immediately prior to the measurements. All spectra were acquired in total electron yield detection mode. Samples were oriented with the [100] and [001] direction in the horizontal plane. X-ray magnetic linear dichroism measurements were performed in normal incidence, i.e. with the incoming X-ray beam along the [001] direction. X-ray magnetic circular dichroism measurements were done in grazing incidence geometry by turning the sample by 60° about the vertical axis with respect to the normal incidence geometry.

F. Resistivity

Electrical transport measurements on the EuMn_2P_2 samples were conducted using an AC four-point probe setup and a lock-in amplifier. Low-resistance electrical contacts were achieved by thermally evaporating 200 nm of gold, with a 7 nm chromium wetting layer, onto the polished crystal surfaces. Gold wires and silver paste were used for electrical connections. To confirm ohmic behavior, I-V measurements were conducted using a standard DC technique at various temperatures. The resistivity was calculated based on the contact geometry and the dimensions of the a - a plane and c axis.

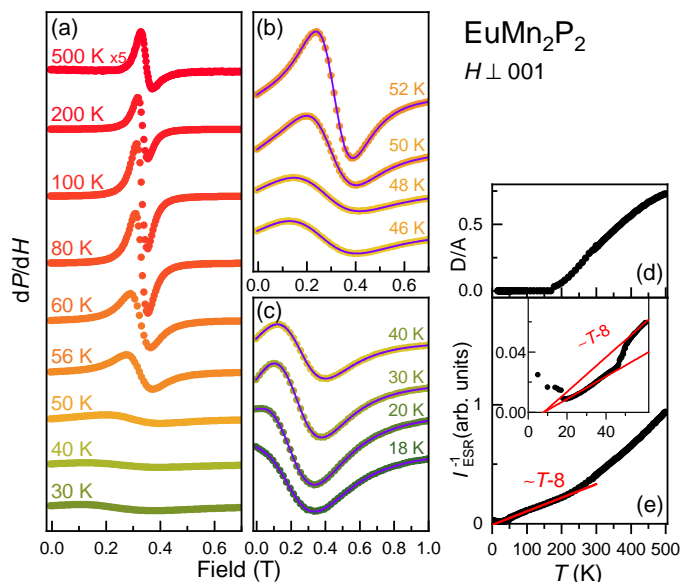


FIG. 2. Typical ESR spectra (first field-derivative of absorbed power) of single crystalline EuMn_2P_2 at X-band (9.4 GHz) and in-plane field direction. (a) Overview for broad temperature region, (b) for region around $T_M = 47\text{ K}$, (c) for region near, but above the magnetic order at T_N . Solid lines in (b) and (c) denote Lorentzian lineshapes. Temperature dependence of (d) lineshape parameter dispersion-to-absorption, D/A , and (e) reciprocal ESR intensity, enlarged in the inset. Solid lines indicate Curie-Weiss laws $(T - \theta_W)^{-1}$.

III. RESULTS

A. Electron spin resonance

The observed ESR signal in EuMn_2P_2 consists of a single and well resolved Lorentzian line in the whole temperature range investigated. At 295 K it corresponds to $g_{\parallel} = 1.984$ ($H \parallel 001$) and $g_{\perp} = 2.003$ ($H \perp 001$), i.e., g -values consistent with an Eu^{2+} resonance as seen in other Eu-pnictides [28–31]. The temperature dependencies of linewidth ΔH and resonance field H_{res} show clear anomalies not only at T_N (Eu-magnetic order) but also at $T_M = 47\text{ K}$ which we relate to Mn spin correlations.

Fig. 2(a-c) shows ESR spectra at selected temperatures in the paramagnetic region. A Lorentzian shape, solid line, describes the spectra perfectly well, in particular in the region around $T_M = 47\text{ K}$, Fig. 2(b), and near Eu-magnetic order at T_N , Fig. 2(c). As will be shown below, an anomalous behavior of linewidth and resonance field appears around T_M . For $T < T_N$ double line spectra appear (not shown) as being characteristic for the magnetic resonance of ordered spin systems [37]. A finite dispersion contribution to the lineshape, $D/A > 0$, appears around $T = 150\text{ K}$, see Fig. 2(d). Above this temperature, the microwave penetration depth falls below the sample size as a consequence of an increasing sample con-

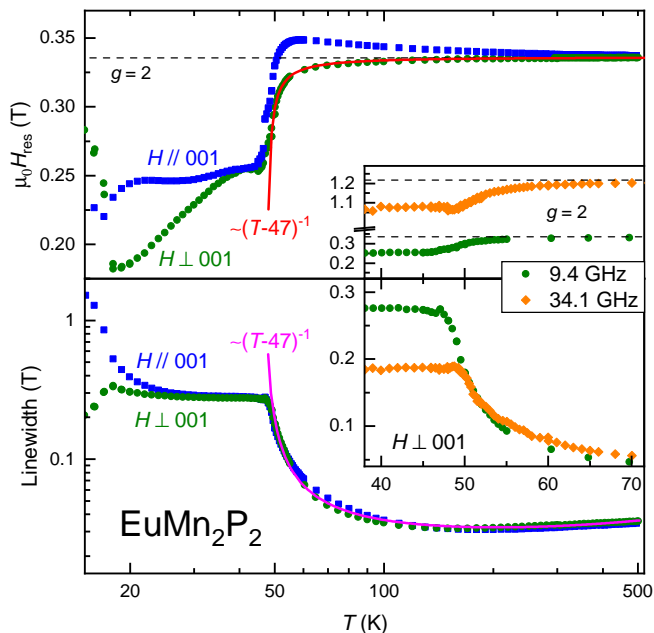


FIG. 3. Temperature dependence of resonance field (top frames) and linewidth (bottom frames) for indicated field directions. Solid lines indicate Curie-Weiss behavior.

ductivity. At $T = 500$ K, $D/A \simeq 0.7$ which is reflected in a clear asymmetry in the lineshape as can be seen in the top spectrum of Fig. 2(a).

The ESR intensity as deduced from the integrated ESR spectra [34] is depicted in Fig. 2(e). A clear kink is visible around $T_M = 47$ K above and below which I_{ESR} is characterized by a Curie-Weiss behavior with $\theta_W = +8$ K. Around 200 K, an upward bending of $I_{\text{ESR}}^{-1}(T)$ is observed. This is most probably due to a microwave skin depth (δ) reduction as indicated by a strong increase of the D/A ratio, see Fig. 2(d). In this case, the approximation in calculating $I_{\text{ESR}}(T)$ (Ref.[34]) is not valid.

The temperature dependencies of the linewidth and the resonance field are depicted in Fig. 3. Both quantities show remarkable shoulder-form anomalies around $T_M = 47$ K. By decreasing the temperature across T_M the line broadening abruptly stops, whereas at the same time the resonance field strongly decreases. These features depend on the applied field, as shown in the inset of Fig. 3. The position of the shoulders shift to higher temperatures when shifting the resonance to higher fields by changing the microwave frequency from 9.4 GHz to 34 GHz. This behavior is also consistently observed in specific heat data. Towards high temperatures, $T \rightarrow 500$ K, the resonance field merges the field corresponding to $g = 2$ (dashed lines in Fig. 3) being a typical value for Eu^{2+} while the linewidth contains a linear contribution, indicating a Korringa relaxation, and a tendency to saturation. The latter indicates exchange narrowing according to the Kubo-Tomita mechanism [38, 39].

The approach from above towards the magnetic order at T_N influences the resonance field to shift in opposite directions for the two field directions applied. This is quite similar to the shift reported for $\text{EuFe}_{2-x}\text{Co}_x\text{As}_2$ where it indicates increasing internal fields near the magnetic order of the Eu spins [31]. For EuMn_2P_2 , the reduction of the resonance field near T_N is strongest for the in-plane field direction, which is consistent with in-plane ferromagnetically correlated Eu^{2+} spins. Approaching T_M from above, the in-plane resonance field reflects the evolution of the in-plane magnetization, showing a Curie-Weiss dependence $\propto (T - 47)^{-1}$ (see red solid line in Fig. 3).

For the linewidth, when decreasing the temperature towards T_N , one typically expects a broadening due to increasing spin correlations. Above $T_M = 47$ K, however, this mechanism obviously is superimposed by the effect of spin correlations related to the anomaly at T_M . These correlations can be described by a $(T - 47)^{-1}$ behavior in the linewidth (see pink solid line in Fig. 3). Thus, the broadening shows a critical behavior with a critical exponent of -1 which is observed in systems with spin fluctuations in a 3D Heisenberg ferromagnet [40].

B. Heat capacity

Fig. 4(a) shows the zero-field heat capacity of EuMn_2P_2 between 2 K and 200 K. At low temperatures, a sharp λ -type anomaly appears with a peak at $T_3 = T_N^{\text{Eu}} = 18$ K, Fig. 4(b), which can be attributed to the Eu^{2+} AFM-order. Fig. S1 [41] shows the field dependence of this transition with the field applied along the out-of-plane direction, $H \parallel 001$, between 11 K and 19 K. An increase in the external magnetic field results in a shift of the transition temperature T_3 towards lower temperatures, which is consistent with an AFM ordering of the Eu^{2+} spins. The peak is completely suppressed for fields exceeding $\mu_0 H = 5$ T. In addition, as shown in Fig. 4(a,c), two small anomalies at $T_2 = 48.5$ K and $T_1 = 51$ K were observed in zero field after precise measurements in the corresponding temperature range where the significant change in the resonance field and linewidth in the ESR data occurs. Surprisingly, in addition to the anomaly at T_2 , a further anomaly was detected in the heat capacity at around T_1 , which was not resolved in the ESR data.

Fig. 5 shows the field-dependent heat capacity close to the T_1 and T_2 transitions for $H \perp 001$ and $H \parallel 001$. The T_1 transition shifts to higher temperatures, and the shift seems to be almost isotropic for field aligned along the two crystallographic directions. In addition, for both field directions the peak at T_1 gets broader with increasing field. In contrast, the peak at T_2 sharpens with increasing field for both directions and presents an anisotropic shift towards higher temperatures. With field aligned along the [001] direction, the shift to higher

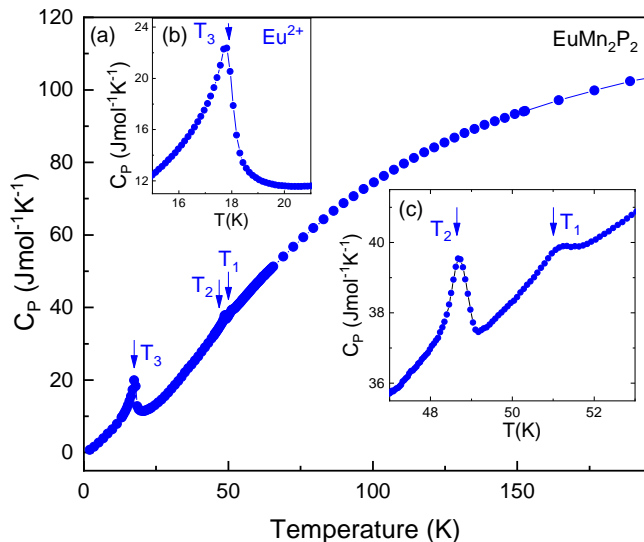


FIG. 4. EuMn_2P_2 (a) Heat capacity at $\mu_0 H = 0$ T as a function of temperature (blue). (b) Enlarged view of the data in the vicinity of the magnetic transition of Eu. (c) Enlarged view of the data in the vicinity of the magnetic transition of T_2 and T_3 .

temperatures is larger compared to the in-plane direction. Our finding is in contrast to the heat capacity results discussed in Ref. [20] where only one Eu^{2+} AFM-transition at T_3 was detected, probably due to the lower T -resolution of those measurements.

Furthermore, to rule out additional transitions the zero-field heat capacity was measured precisely at higher temperatures (see Fig. S2 [41]) comprising the T region around $T = 150$ K where a reoccurring change in slope in the resistivity data was observed as discussed later. However, no further transitions were found between $T = 50 - 200$ K.

C. Magnetic susceptibility and magnetization

The magnetic behavior of EuMn_2P_2 was analyzed by measuring the magnetic susceptibility and magnetization at different magnetic fields. Fig. 6(a) shows the molar magnetic susceptibility $\chi(T)$ of EuMn_2P_2 at $\mu_0 H = 0.1$ T for the in-plane ($H \parallel 210$, $H \parallel 100$) and the out-of-plane directions ($H \parallel 001$). The data exhibit a clear magnetic transition at $T_3 = 18$ K arising from AFM ordering of the Eu^{2+} spins. Furthermore, an anisotropy of the in-plane and out-of-plane directions is seen below T_3 . This is in contrast to the data in [20] where a different kind of anisotropy was detected. The temperature-dependent magnetic susceptibility with various fields applied along the in-plane and out-of-plane directions is depicted in Fig. S3 [41]. The AFM nature of the Eu^{2+} -transition is confirmed by the shift of T_3 with increasing field towards lower temperatures for both field directions. The drop

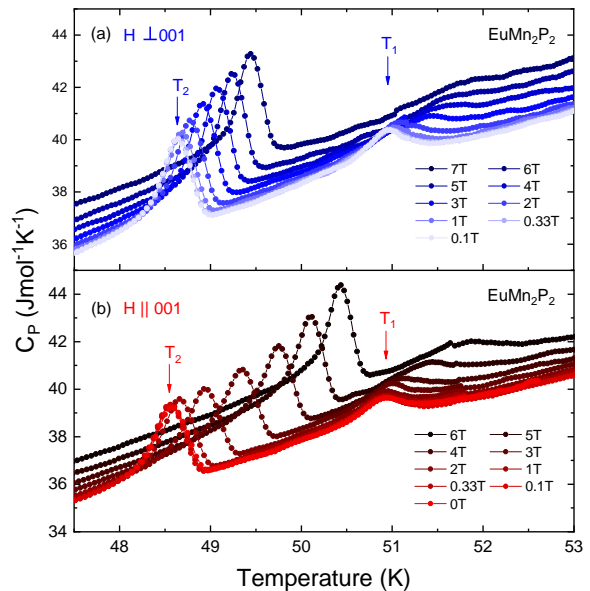


FIG. 5. Heat capacity of EuMn_2P_2 measured in different magnetic fields (a) $H \perp 001$ and (b) $H \parallel 001$ between 47 K and 53 K as a function of temperature. The magnetic transitions at T_1 and T_2 are assigned to a weak ordering of Mn. The peak at T_1 shifts to higher temperatures and broadens in field. In contrast, the peak at T_2 sharpens in field, shifts to higher temperatures with increasing field, and shows an anisotropy for the in-plane and out-of-plane directions.

in the susceptibility at 3.7 K at low fields results from superconducting Sn inclusions inside the sample. The Sn content can vary significantly between samples, with values ranging from (1-5)%.

Fig. S4 [41] shows the reciprocal magnetic susceptibility $\chi^{-1}(T)$ as a function of temperature for the in-plane and out-of-plane directions in the range of 2-300 K measured with an applied magnetic field of $\mu_0 H = 1$ T. The data was fitted using the Curie-Weiss law $\chi^{-1} = (T - \Theta_W)/C$ with a Curie constant $C = 110 \text{ m}^3\text{K/mol}$, between 150 K and 290 K, which leads to an effective moment of $\mu_{\text{eff}} = (8.4 \pm 0.1) \mu_B$ per formula unit and a Weiss temperature $\Theta_W = (7 \pm 1) \text{ K}$ for field along the [001] direction and of $\mu_{\text{eff}} = (8.4 \pm 0.1) \mu_B$ and $\Theta_W = (10 \pm 1) \text{ K}$ for field along an in-plane direction in agreement with [20]. The experimental effective moment is therefore slightly larger compared to the free-ion value of $7.94 \mu_B$ for divalent europium, which may be an indication for further contributions to the magnetic susceptibility from the Mn spins. Below ≈ 130 K, we observe a minor deviation from Curie-Weiss behavior which would be consistent with a development of short-range Mn magnetic correlations which was already discussed in Ref. [20].

Fig. 6(b) shows $\chi(T)$ in the vicinity of the observed T_1 and T_2 anomalies as detected in the heat capacity (Fig. 5). However, no clear feature was seen around the T_1 and T_2 transition temperatures in $\chi(T)$. Mainly, a slight change in slope is observed. The same tempera-

ture range was furthermore measured in field-cooled (FC) and zero-field cooled (ZFC) mode for both field directions (Fig. S5 [41]). Also here, no clear feature was observed around the T_1 and T_2 transitions.

Fig. S6(a) [41] shows the field-dependent magnetic moment $M(H)$ per Eu for field aligned along the different crystallographic orientations at 4 K. The saturation magnetization value is evaluated as $7\mu_B$ at $\mu_0H = 8$ T and 4 K. The sample mass was corrected according to the amount of Sn inclusions inside the sample, as estimated from the drop of $\chi(T)$ below the superconducting transition of Sn (Fig. S3 [41]). The in-plane directions behave nearly isotropic and make the magnetic easy plane of the system with a critical field of $\mu_0H_c^{100} = 4.7$ T. In the out-of-plane direction, the saturation magnetization is reached at a critical field of $\mu_0H_c^{001} = 5.5$ T. The low-field behavior of the moment per Eu^{2+} for the three main symmetry directions, presented as M/μ_0H versus μ_0H is shown in Fig. S6(b) [41]. From these data, it is possible to deduce information about the alignment of the Eu magnetic moments in the ground state of the material. Our result hints to moment alignment close to the [100] direction and is consistent with neutron diffraction which revealed A-type AFM Eu order with moments lying in the $a - a$ plane at 1.4 K with FM coupling in the plane and AFM coupling of the nearest-neighbour spins along the c axis [19].

A hysteresis opens between $\mu_0H = 2.5$ T and 4 T for both field directions, which becomes larger at 10 K, Fig. S6(c) [41]. For the in-plane direction, this hysteresis is more pronounced. Figs. S7 and S8 [41] show the $M(H)$ data for different higher temperatures, especially those collected in the temperature range of the T_1 and T_2 transitions with field along the [001] direction. The $M(H)$ data are almost linear in H at each temperature, and no significant change in slope was detected at the transition temperatures.

D. Nuclear magnetic resonance

The NMR spectra of a polycrystalline powder sample of EuMn_2P_2 were investigated at a fixed frequency $\nu = 40$ MHz in the temperature range between 300 K and 40 K. The results are shown in Fig. 7. The spectra show a characteristic pattern of randomly oriented powder sample in a layered environment. The lineshape was simulated to extract the shift values according to the $a - a$ plane ${}^{31}\text{K}_{aa}$ and c direction ${}^{31}\text{K}_c$, respectively. The inset shows a simulation together with the data for 175 K. The ${}^{31}\text{P}$ NMR line shows a negative total shift with a slightly larger value perpendicular to the $a - a$ plane. The shift values increase towards lower temperatures, and the anisotropy becomes less visible below approximately 125 K. Towards lower temperatures, a broadening of the line could be seen. Below 40 K, a measurement of the ${}^{31}\text{P}$ NMR signal becomes very complicated due to the fact that the relax-

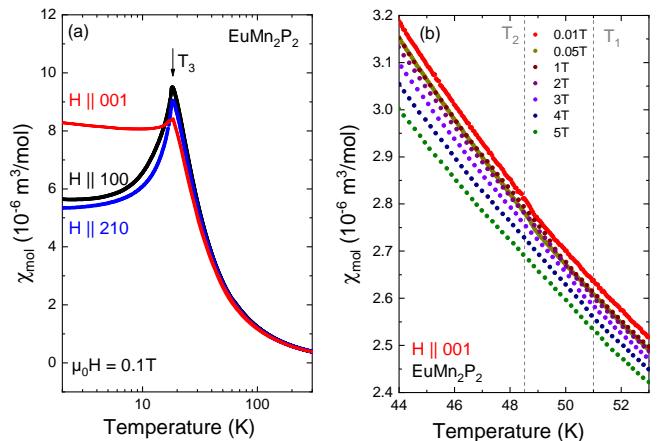


FIG. 6. (a) Molar magnetic susceptibility $\chi_{\text{mol}}(T)$ at $\mu_0H = 0.1$ T for $H \parallel 100$, $H \parallel 210$ and $H \parallel 001$. (b) $\chi_{\text{mol}}(T)$, $H \parallel 001$: The two magnetic transitions at T_1 and T_2 are hardly visible in the magnetic susceptibility. Dashed lines indicating the transition temperatures from the zero field HC are guides to the eyes.

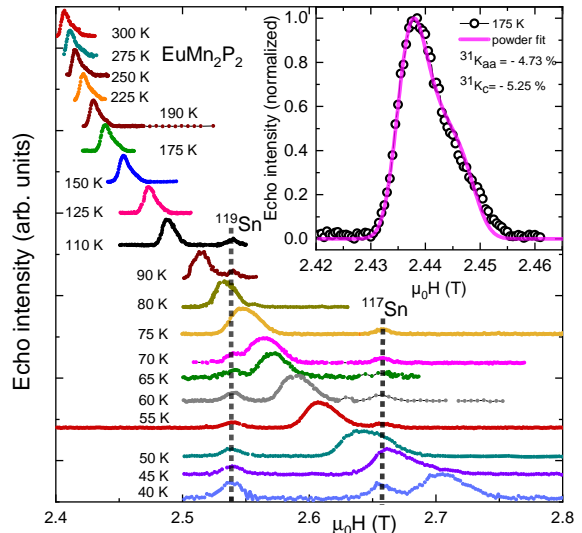


FIG. 7. ${}^{31}\text{P}$ field sweep NMR spectra taken at 40 MHz at various temperatures as indicated. The spectra were normalized to the maximum signal of the ${}^{31}\text{P}$ NMR line (of each individual spectra) and shifted by a constant value in the vertical direction for better clarity. The vertical dotted lines indicates the Larmor fields for ${}^{119,117}\text{Sn}$. The ${}^{31}\text{P}$ NMR line shows a sizable shift and broadening towards lower temperatures, whereas the ${}^{119,117}\text{Sn}$ lines does not show any temperature dependent shift, as expected for a Sn containing non-magnetic impurity. The inset shows the ${}^{31}\text{P}$ NMR line at 175 K together with a theoretical powder simulation (solid line).

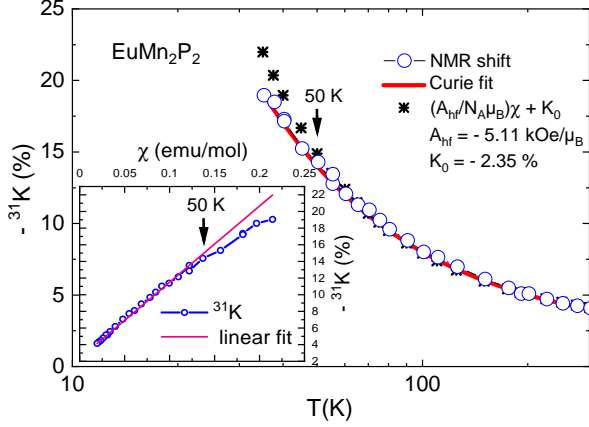


FIG. 8. Temperature dependence of the ^{31}P isotropic shift $^{31}K_{\text{iso}}$ in EuMn_2P_2 estimated from 40 MHz field sweep NMR. The curved line indicates a Curie fit to the data (see text). The star symbols correspond to shift values calculated from the determined hyperfine coupling constant. The inset shows the K - χ plot together with a linear fit above 50 K. Note that here the susceptibility at 2.45 T was used.

ation becomes very fast and the signal wipes out. Before we discuss the wipe out effect, we discuss the temperature dependent shift.

The transferred hyperfine field at the P ligand site originates mainly from the Eu and Mn based magnetism. As usual we have a combination of mechanisms for the transfer. Conduction electron polarization, core polarization through d electrons and superexchange are usually discussed to originate the hyperfine field at the ligand site. The hyperfine field causes a shift of the NMR line with respect to the nonmagnetic reference compound. Usually the temperature dependent part of the shift is related to the bulk susceptibility via the hyperfine coupling constant. In addition, a small temperature independent part is frequently found which could be related either to conduction electrons (positive) or orbital contributions (negative).

The total Knight shift can be described by a sum of two contributions:

$$\mathcal{K} = \mathcal{K}_0 + \mathcal{K}_{4f/3d}(T). \quad (1)$$

The temperature dependent shift contribution is related to the bulk susceptibility, giving:

$$\mathcal{K}_{4f/3d}(T) = \frac{A_{\text{hf}}}{N_A \mu_B} \chi(T), \quad (2)$$

where A_{hf} is the hyperfine coupling constant, N_A the Avogadro number and μ_B the Bohr magneton [42]. We used phosphorous acid H_3PO_4 with $^{31}\text{K} = 0$ as a reference compound for the absolute shift determination. Fig. 8 shows the isotropic shift given by $^{31}K_{\text{iso}} = (2K_{a,b} +$

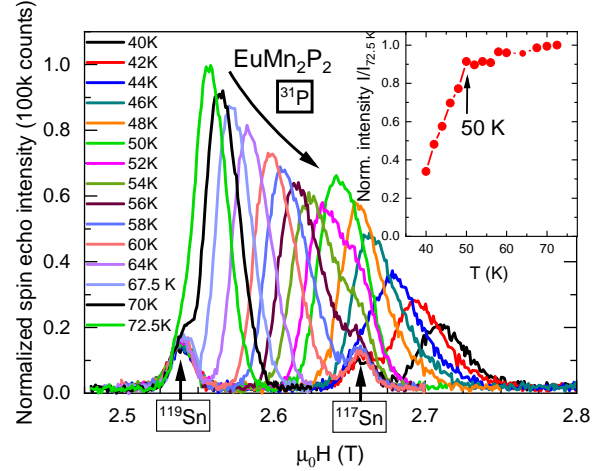


FIG. 9. ^{31}P field sweep NMR spectra taken with an increased number of scans in a narrow temperature window between 72.5 K and 40 K. The spectra were normalized to the maximum signal of the ^{31}P NMR line at 72.5 K. A strong decrease of the maximum signal is clearly visible. The integration of the signal vs field of the individual ^{31}P NMR line gives the NMR intensity at each temperature. The NMR intensity of the ^{31}P sweep NMR line is plotted in the inset as function of temperature (note that this is normalized to the intensity as 72.5 K).

$K_c)/3$ as a function of temperature. The "Clogston-Jaccarin" plot (K - χ plot, see Fig. 8 inset) relates the NMR shift $^{31}K_{\text{iso}}$ to the bulk susceptibility of the polycrystalline sample. We obtain the hyperfine coupling constant of $A_{\text{hf}} = -5.11 \text{ kOe}/\mu_B$ from the observed linearity of this plot and a K_0 value of -2.35%.

Fig. 9 shows the ^{31}P NMR line always recorded with the same number of scans at various temperatures between 72.5 K and 40 K. Even from these plots, it becomes clear that the line is strongly suppressed towards low temperatures. The NMR intensity is given by the in-field integration over the NMR line (Note that we corrected for the intensities of the $^{119,117}\text{Sn}$ lines.) and it is plotted as function of temperature in the inset of the figure. It becomes rather clear that we lose 2/3 of the intensity while going down from 72.5 K to 40 K and that the decay sets in at about 50 K as shown in the inset of Fig. 9. The full width half maximum (FWHM) of the ^{31}P NMR line as a function of temperature is shown in Fig. S10 in the SI [41].

E. X-ray magnetic circular and linear dichroism

Having established the existence of weak order which is of magnetic origin through ESR, HC and NMR, we now attempt to gain further information about the transitions at $T_{1,2}$. For the element specific magnetic charac-

terization we measured the circular and linear magnetic dichroism in the Mn $L_{3,2}$ and Eu $M_{5,4}$ X-ray absorption spectra as a function of applied magnetic field and temperature. Fig. 10 shows the X-ray magnetic circular dichroism (XMCD) for both edges at $T = 23$ K and an applied field of $\mu_0 H = 9$ T. In XMCD, the magnetic field is applied along the X-ray beam, $H \parallel c$, and the size of the XMCD signal is proportional to the component of the magnetic moment aligned along the field. Using the XMCD sum rules, we find an aligned magnetic moment of $\mu_{\text{Eu}} = \mu_{\text{S}} = 5.6 \mu_B$ at 9 T, in agreement with the total magnetic moment per f.u. observed in the bulk magnetization measurements at this temperature. The sum rule analysis yields a pure spin moment with no orbital contribution as expected for Eu^{2+} ions. For the Mn ions, we find only a very small XMCD signal at $T = 23$ K and $\mu_0 H = 9$ T. A precise application of the XMCD sum rules for Mn is usually prohibited by the too small separation between the Mn L_3 and L_2 absorption edges. However, we can still use the sum rules to estimate an upper limit for the total Mn magnetic moment aligned by the applied field and the spin vs orbital contribution to this moment. We find a very small, pure spin moment without a detectable orbital contribution: $\mu_{\text{Mn}} = \mu_{\text{S}} < 0.03 \mu_B$.

In Fig. 10 (c), we show the field dependence of the Eu and Mn XMCD signal below and above T_3 . The Eu XMCD signal is again in good agreement with the bulk $M(H)$ measurements. The Mn XMCD signal follows the field dependence observed for Eu within the error bars set by the very small Mn XMCD signal, both in the Eu AFM and paramagnetic phase. The observation of an only very small, pure spin Mn magnetic moment following closely the Eu magnetization could be compatible with an induced magnetic moment at the Mn sites due to the large Eu magnetic moments.

In Fig. 11, we present the X-ray magnetic linear dichroism (XMLD) at the Eu $M_{5,4}$ and Mn $L_{3,2}$ edges as a function of temperature for normal incidence, i.e. the incident X-ray beam parallel to [001].

In this geometry, the XMLD signal is the difference in the absorption for two orthogonal linear X-ray polarizations in the $a - a$ plane, one along [100] and one perpendicular to it. It is sensitive to the projection of staggered magnetic moments along the two polarization directions, and therefore suitable to detect FM and AFM order alike. In normal incidence geometry it can be used to probe the in-plane component of a potential Mn magnetic order. We can detect a clear XMLD signal at the Eu M_5 edge with a strong temperature dependence between 5 K to 18 K, in agreement with the T_3 detected by other techniques. In addition to this clear temperature dependence in zero applied field, we further confirmed the magnetic origin of the detected signal by applying a magnetic field at $T = 5$ K. With an applied magnetic field of $\mu_0 H = 0.4$ T along [100] we observed an enhancement of the XMLD signal, in agreement with the expectation of going to-

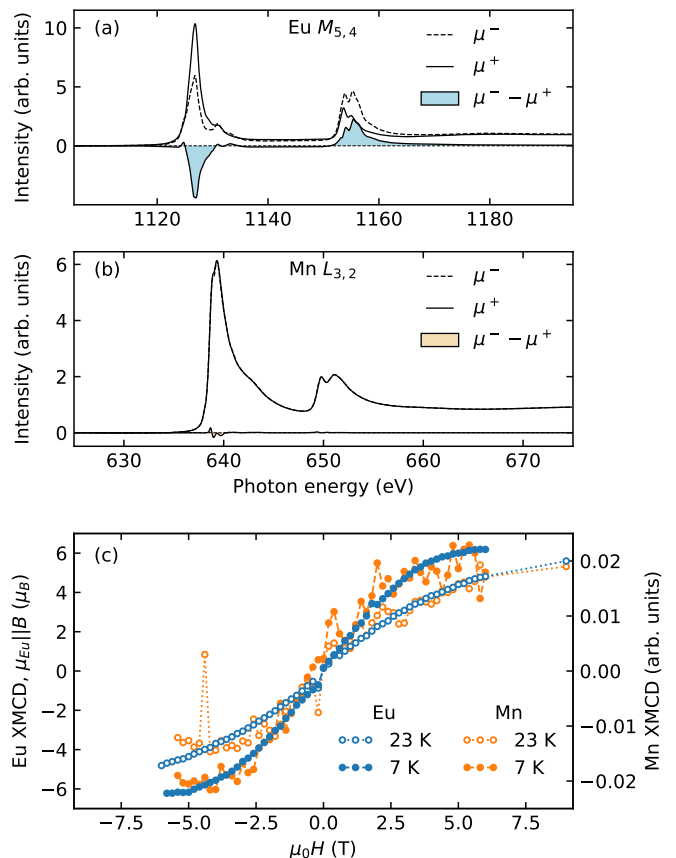


FIG. 10. (a) XMCD spectra taken at $T = 23$ K at the Eu $M_{5,4}$ edges, (b) the Mn $L_{3,2}$ edges, and (c) the magnetic field dependence of the XMCD signal at both edges for $T = 23$ K ($T > T_3$) and $T = 7$ K ($T < T_3$).

wards a single domain AFM state with moments parallel to [100]. Also in agreement with expectation, applying 9 T along [001] and aligning the Eu moments along this direction suppressed the XMLD signal.

In contrast to Eu, no clear Mn XMLD signal was found within the detection limit of the experiment, even after application of 0.4 T along [001]. This was true both below T_3 as well as above T_3 at $T = 33$ K and $T = 51$ K.

F. Resistivity

Fig. 12(a) depicts the resistivity measured with an AC current applied in the $a - a$ plane of EuMn_2P_2 on a logarithmic scale versus temperature. At room temperature the sample is well conducting with a resistivity of $\rho(T = 300 \text{ K}) \approx 2 \Omega\text{cm}$. Upon cooling down the resistivity increases exponentially as illustrated in the Arrhenius plot in the inset. For high temperatures, a linear fit provides an excellent description of the data, yielding an activation energy of $E_A = 213 \text{ meV}$, in agreement with [20]. However, at $T = 142$ K the slope changes, resulting in the emergence of a shoulder-like feature, which

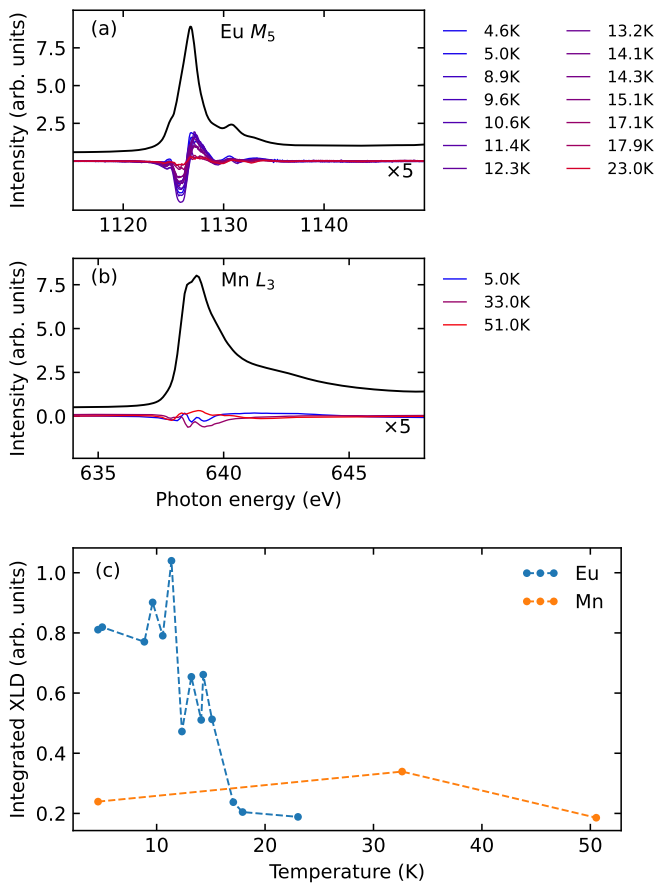


FIG. 11. XMLD spectra taken at normal incidence and zero field for Eu (a), at $\mu_0 = 0.4$ T applied along [100] for Mn (b) as well as the temperature dependence of both the Eu and Mn XMLD signals (c).

appears to be sample dependent, Fig. S9. In the same temperature range short-range magnetic correlations of Mn were observed [20]. At lower temperatures, the resistivity further increases, indicating a continuing, albeit now very weak semiconducting behavior. The blue curve was obtained in an external field of $\mu_0 H = 10$ T applied along the c -direction. As illustrated by Fig. 12(b), applying a magnetic field along the c -direction does not result in a significant alteration of the overall temperature behavior of the resistivity. This is in stark contrast to analogous compounds such as EuCd_2P_2 [4] and EuZn_2P_2 [7], which exhibit a colossal magnetoresistance behavior at low temperatures. The difference between the $\mu_0 H = 10$ T and the zero field measurements is plotted in red, where a small negative magnetoresistance of the order of a few percent between $T = 200$ K and $T = 100$ K is observed. The inset presents various magnetic fields between 0 and 10 T, demonstrating a small but systematic shift of the resistivity within this temperature range with increasing magnetic field.

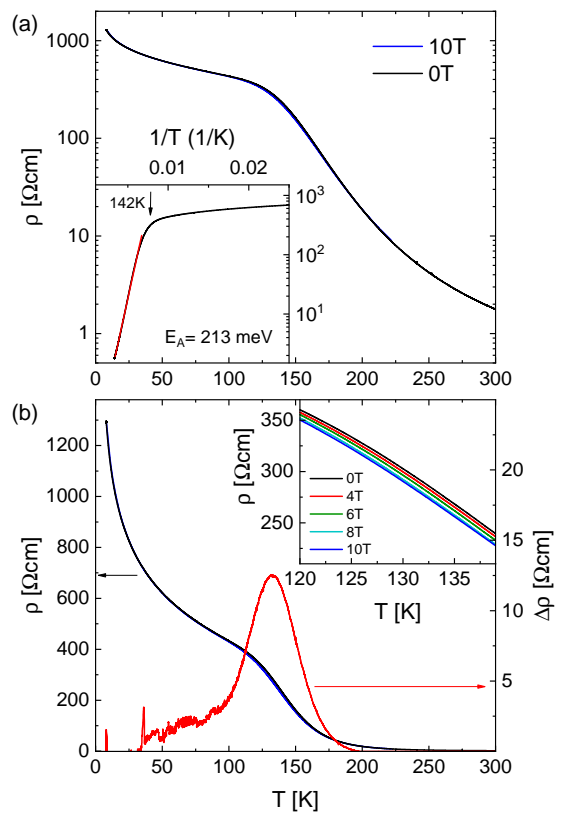


FIG. 12. (a) Temperature dependent resistivity with an AC current applied in the a - a plane of EuMn_2P_2 on a logarithmic scale measured at 0 and 10 T. The inset shows the Arrhenius plot with a calculated activation energy of $E_A = 213$ meV. (b) Temperature dependent resistivity for 10 T (blue curve) and the difference between the 10 T and 0 T curve (red curve).

IV. DISCUSSION

The most intriguing property of the observed spin resonance in EuMn_2P_2 appears when crossing $T_M = 47$ K where the temperature dependencies show clear anomalies in the linewidth, the resonance field, and the intensity while the lineshape is preserved. Such anomalies are not reported for isostructural EuZn_2P_2 where non-magnetic Zn replaces the Mn sites [27]. We therefore suspect that the observed anomalies are related to an Eu^{2+} resonance which is coupled to the Mn spin system. Above $T = T_M$, the Eu relaxation involves Mn spins which have itinerant character as the states near the Fermi level are dominated by Mn in the $(\text{Mn}_2\text{P}_2)^{2-}$ layers [20]. This itinerancy is reflected in the ESR spectra as a finite dispersion of the lineshape and in a weak Korringa, linear in T linewidth contribution. The Mn spin system has a characteristic temperature T_M where short range Mn order might set in. Approaching T_M from above, critical Mn-spin fluctuations lead to a broadening of the Eu line $\propto (T - T_M)^{-1}$. Upon decreasing the temperature below T_M , the relaxation towards the Mn spin bath is effectively canceled, leading then to the observed kink in the Eu linewidth

and to a suppression of the effective Eu-resonance field because of the evolving internal Mn field.

Given the fact, that the signals at T_1 and T_2 detected in the heat capacity are very small, we attribute these high temperature transitions to the weak ordering of the Mn spins in their triangular environment, which might be hindered due to magnetic frustration. The calculated entropy contribution is $S = 0.035 \text{ Jmol}^{-1}\text{K}^{-1}$, which represents only 0.6% of the expected value of $R\ln 2$ for a local Mn ordering. For fields higher than $\approx 1 \text{ T}$, the peak at T_1 starts broadening and shifting to slightly higher temperature, which hints to a ferromagnetic component of the weak Mn order. This emerging weak magnetic order at T_1 appears to shift isotropically to higher temperatures with applied magnetic field and is followed by a further transition at T_2 for which we observe an anisotropic increase, when applying the magnetic field along the two different directions. In case of a simple ferromagnetic transition, one expects a strong broadening already at low magnetic fields, ruling out purely ferromagnetic ordering of the Mn spins at the T_2 phase transition. We neither observe a suppression of the transition at T_2 in field which would indicate simple AFM order. Instead, the peak at T_2 is stabilized in field which hints to a scenario where frustration of the Mn-moments situated on a triangular lattice in this crystal structure might play a role. This order might be suppressed based on anisotropic magnetic interactions due to the layered Mn system. Furthermore, the observed magnetic field dependencies of the anomalies rule out the possibility of purely structural origin of the transitions at T_1 and T_2 .

Already below $\approx 130 \text{ K}$, we observe a minor deviation of $\chi^{-1}(T)$ from the fit according to the Curie-Weiss law, which is consistent with [20] where the development of Mn magnetic fluctuations is described in a similar temperature range. In $\chi(T)$, a minor change of slope is observed around the T_1 and T_2 transitions only. Nevertheless, a comparison of the EuMn_2P_2 data with those reported earlier for the non-magnetic compounds, $(\text{Sr,Ca})\text{Mn}_2\text{P}_2$ [43], would suggest that any contributions of the Mn atoms to the magnetic susceptibility would be of the order of magnitude of $10^{-10} \text{ m}^3/\text{mol}$, which in this temperature range is four order of magnitudes lower compared to the paramagnetic signal from the Eu-moments. This makes it almost impossible to discern weak 3d-based magnetic signatures on the background of an Eu^{2+} system. The minor contribution to the magnetic susceptibility might be attributed to spin fluctuations, which stem from the quasi-two-dimensional nature of the Mn spin layers, along with a possible contribution from magnetic frustration. A similar behavior was observed in CaMn_2P_2 and SrMn_2P_2 , where the magnetic susceptibility increases with temperature, showing a broad maximum unlike most local moment antiferromagnets [43]. The magnitude of the hyperfine coupling constant as determined by NMR is common for 4f local moment metals [44, 45]. It should be mentioned that the utilized model is only valid down to approximately 50 K. Below that

temperature, the breakdown of the linearity in \mathcal{K} vs χ (inset of Fig. 8) indicates a change of the magnetic correlations in the system (where A_{hf} becomes T -dependent). This might be taken as a fingerprint of the hidden 3d-Mn-based magnetism. There is also a discontinuous behavior of the linewidth of the ^{31}P NMR line, which also might indicate the presence of small Mn based magnetism. Another hint towards the presence of weakly Mn-based magnetism embedded in the predominant local moment 4f Eu based paramagnetism comes from the NMR intensity itself.

Based on this, we speculate that around 50 K the Mn based magnetism is altered, probably undergoes either long range or short range order, and the associated critical fluctuations are responsible for the signal wipe out effect found in NMR. From the linewidth change below 100 K and the determined hyperfine coupling constant, we estimated an upper limit of the moment variation of about $0.06\mu_B$. This indicates a rather small effect which is not visible in the NMR shift or bulk susceptibility but in the magnetic relaxation process (leading to the wipe out) and in the line broadening. For EuMn_2P_2 there is only one ^{31}P NMR study on polycrystalline samples above 100 K [20]. The data determined there are in reasonable agreement with our data although they were determined in a larger magnetic field (frequency). Absolute shift values and the hyperfine coupling constant ($-4 \text{ kOe}/\mu_B$) are close to ours ($-5.11 \text{ kOe}/\mu_B$). In contrast, the pure Mn-based system SrMn_2P_2 has very small shift values, which is due to the weak Mn magnetism [43]. However, the hyperfine interaction constant determined there ($-5.23 \text{ kOe}/\mu_B$) is comparable to the constant determined by us in EuMn_2P_2 ($-5.11 \text{ kOe}/\mu_B$).

The results of ESR, heat capacity, magnetization, and NMR convincingly show the presence of weak Mn order below 51 K. Using XMCD, we find a very small, pure spin moment of $\mu_{\text{Mn}} = \mu_{\text{S}} < 0.03\mu_B$ without a detectable orbital contribution, which follows closely the Eu magnetization in field. This could be compatible with an induced magnetic moment at the Mn sites due to the large Eu magnetic moments. No evidence of Mn order independent of Eu can be found in the XMCD data, within the detection limits of the measurement. Also, no clear Mn XMLD signal was found below the $T_{1,2}$ transitions or in the AFM ordered phase of Eu.

One possibility why no clear magnetic ordering of Mn was found in XMLD could be, that Mn orders completely out of plane and 0.4 T cannot realign it in the plane. In this case, Mn would not give an XMLD signal in the used geometry. We should also keep in mind the potential influence of the surface in the discussed X-ray magnetic dichroism experiments. In that regard, there are examples, like GdRh_2Si_2 or EuRh_2Si_2 , where surface and bulk show different ordering temperatures [46], [47] or others, like HoIr_2Si_2 , where despite AFM order of the bulk [48], no magnetic order of the surface could be

detected (unpublished data).

The magnetic transitions of the material are also not visible in the electrical transport data. Interestingly, the resistivity exhibits a change of slope at 142 K which indicates a change of the band structure near the temperature where in the inverse magnetic susceptibility a slight deviation from the Curie-Weiss behavior is observed which is probably connected to the onset of magnetic fluctuations of Mn.

V. SUMMARY

We investigated the electron spin resonance of EuMn_2P_2 and, besides the antiferromagnetic transition of Eu at 18 K, we found an additional feature at 47 K which is of magnetic origin. The ESR temperature dependencies show clear anomalies in the linewidth, the resonance field, and the intensity, while the lineshape is preserved when crossing $T_M = 47$ K. Using heat capacity, we could resolve two small subsequent transitions T_1 and T_2 in the same temperature range. The transition at $T_1 = 51$ K is isotropic for field along the two crystallographic main symmetry directions, shifts to higher temperatures and broadens in field which hints to its possibly ferromagnetic nature. Given the small size of the signal, we attribute this transition to a possible order of the Mn spins. The transition at $T_2 = 48.5$ K is anisotropic, gets enhanced and shifts to higher T in field. This particular behavior at the transition is probably caused by magnetic frustration favored by the

trigonal arrangement of the Mn sublattice. Using NMR, we can give an upper limit for the small moment of Mn of only $0.06 \mu_B$. This small magnetic contribution emerging at $T_{1,2}$ on a large paramagnetic background of the Eu spins is in accordance with the electrical resistivity of EuMn_2P_2 showing no sign of the putative ordering of Mn. While ESR and NMR are consistent with an evolving internal field of Mn at $T_1 = 51$ K, no direct evidence for Mn order is detected via XMCD or XMLD in the same temperature range which might be due to the small size of the magnetic moment, with a potential c -component or frustration. Our susceptibility and electrical transport data are consistent with the conclusion of a possible onset of Mn fluctuations below ≈ 150 K which was drawn in a previous report [20]. From density functional theory calculations presented in Ref. [20] it was concluded that if Mn order occurs, then it should be AFM. This is not supported by our heat capacity data, which rather hints to a FM nature of the Mn order at T_1 . Further theoretical studies will be necessary in the future in order to fully understand the entire scenario in the EuMn_2P_2 system.

VI. ACKNOWLEDGMENTS

We thank T. Förster for technical support. We thank C. Geibel, R. Valentí, A. Böhmer and H.-A. Krug von Nidda for valuable discussions and acknowledge funding by the Deutsche Forschungsgemeinschaft (DFG, German Research Foundation) via the SFB/TRR 288 (422213477, project A03, A10, B02).

-
- [1] J.-Z. Ma, S. M. Nie, C. J. Yi, J. Jandke, T. Shang, M. Y. Yao, M. Naamneh, L. Q. Yan, Y. Sun, A. Chikina, V. N. Strocov, M. Medarde, M. Song, Y.-M. Xiong, G. Xu, W. Wulfhel, J. Mesot, M. Reticcioli, C. Franchini, C. Mudry, M. Müller, Y. G. Shi, T. Qian, H. Ding, and M. Shi, *Science Advances* **5**, eaaw4718 (2019).
- [2] L.-L. Wang, N. H. Jo, B. Kuthanazhi, Y. Wu, R. J. McQueeney, A. Kaminski, and P. C. Canfield, *Phys. Rev. B* **99**, 245147 (2019).
- [3] H. Su, B. Gong, W. Shi, H. Yang, H. Wang, W. Xia, Z. Yu, P.-J. Guo, J. Wang, L. Ding, L. Xu, X. Li, X. Wang, Z. Zou, N. Yu, Z. Zhu, Y. Chen, Z. Liu, K. Liu, G. Li, and Y. Guo, *APL Materials* **8**, 011109 (2020).
- [4] Z.-C. Wang, J. D. Rogers, X. Yao, R. Nichols, K. Atay, B. Xu, J. Franklin, I. Sochnikov, P. J. Ryan, D. Haskell, and F. Tafti, *Advanced Materials* **33**, 2005755 (2021).
- [5] V. Sunko, Y. Sun, M. Vranas, C. C. Homes, C. Lee, E. Donoway, Z.-C. Wang, S. Balguri, M. B. Mahendru, A. Ruiz, B. Gunn, R. Basak, S. Blanco-Canosa, E. Schierle, E. Weschke, F. Tafti, A. Frano, and J. Orenstein, *Phys. Rev. B* **107**, 144404 (2023).
- [6] D. Y. Usachov, S. Kreyber, K. A. Bokai, A. V. Tarasov, M. Kopp, C. Garg, A. Virovets, J. Müller, M. Mende, G. Poelchen, D. V. Vyalikh, C. Krellner, and K. Kliemt, *Phys. Rev. B* **109**, 104421 (2024).
- [7] S. Kreyber, M. Kopp, C. Garg, K. Kummer, J. Sichelschmidt, S. Schulz, G. Poelchen, M. Mende, A. V. Virovets, K. Warawa, M. D. Thomson, A. V. Tarasov, D. Y. Usachov, D. V. Vyalikh, H. G. Roskos, J. Müller, C. Krellner, and K. Kliemt, *Phys. Rev. B* **108**, 045116 (2023).
- [8] K. Singh, S. Dan, A. Ptok, T. A. Zaleski, O. Pavlosiuk, P. Wiśniewski, and D. Kaczorowski, *Phys. Rev. B* **108**, 054402 (2023).
- [9] S. Luo, Y. Xu, F. Du, L. Yang, Y. Chen, C. Cao, Y. Song, and H. Yuan, *Phys. Rev. B* **108**, 205140 (2023).
- [10] F. Du, L. Yang, Z. Nie, N. Wu, Y. Li, S. Luo, Y. Chen, D. Su, M. Smidman, Y. Shi, C. Cao, F. Steglich, Y. Song, and H. Yuan, *npj Quantum Materials* **7**, 65 (2022).
- [11] X. Cao, J.-X. Yu, P. Leng, C. Yi, X. Chen, Y. Yang, S. Liu, L. Kong, Z. Li, X. Dong, Y. Shi, M. Bibes, R. Peng, J. Zang, and F. Xiu, *Phys. Rev. Res.* **4**, 023100 (2022).
- [12] K. Singh, O. Pavlosiuk, S. Dan, D. Kaczorowski, and P. Wiśniewski, *Phys. Rev. B* **109**, 125107 (2024).
- [13] H. Zhang, J.-T. Zhao, Y. Grin, X.-J. Wang, M.-B. Tang, Z.-Y. Man, H.-H. Chen, and X.-X. Yang, *The Journal of Chemical Physics* **129**, 164713 (2008).

- [14] H. Zhang, L. Fang, M.-B. Tang, H.-H. Chen, X.-X. Yang, X. Guo, J.-T. Zhao, and Y. Grin, *Intermetallics* **18**, 193 (2010).
- [15] E. Gati, S. L. Bud'ko, L.-L. Wang, A. Valadkhani, R. Gupta, B. Kuthanazhi, L. Xiang, J. M. Wilde, A. Sapkota, Z. Guguchia, R. Khasanov, R. Valenti, and P. C. Canfield, *Phys. Rev. B* **104**, 155124 (2021).
- [16] N. H. Jo, B. Kuthanazhi, Y. Wu, E. Timmons, T.-H. Kim, L. Zhou, L.-L. Wang, B. G. Ueland, A. Palasyuk, D. H. Ryan, R. J. McQueeney, K. Lee, B. Schrunck, A. A. Burkov, R. Prozorov, S. L. Bud'ko, A. Kaminski, and P. C. Canfield, *Phys. Rev. B* **101**, 140402 (2020).
- [17] X. Chen, Z. Wang, Z. Zhou, W. Yang, Y. Liu, J.-Y. Lu, Z. Ren, G.-H. Cao, F. Tafti, S. Dong, and Z.-C. Wang, *Phys. Rev. B* **109**, 224428 (2024).
- [18] X. Chen, W. Yang, J.-Y. Lu, Z. Zhou, Z. Ren, G.-H. Cao, S. Dong, and Z.-C. Wang, *Phys. Rev. B* **109**, L180410 (2024).
- [19] A. C. Payne, A. E. Sprauve, M. M. Olmstead, S. M. Kauzlarich, J. Y. Chan, B. Reisner, and J. Lynn, *Journal of Solid State Chemistry* **163**, 498 (2002).
- [20] T. Berry, N. Varnava, D. H. Ryan, V. J. Stewart, R. Rasta, I. Heinmaa, N. Kumar, W. Schnelle, R. Bhandia, C. M. Pasco, N. P. Armitage, R. Stern, C. Felser, D. Vanderbilt, and T. M. McQueen, *Journal of the American Chemical Society* **145**, 4527 (2023), pMID: 36789888.
- [21] V. K. Anand and D. C. Johnston, *Phys. Rev. B* **94**, 014431 (2016).
- [22] I. Schellenberg, M. Eul, W. Hermes, and R. Pöttgen, *Zeitschrift für anorganische und allgemeine Chemie* **636**, 85 (2010).
- [23] T.-H. Han, J. S. Helton, S. Chu, D. G. Nocera, J. A. Rodriguez-Rivera, C. Broholm, and Y. S. Lee, *Nature* **492**, 406 (2012).
- [24] A. Banerjee, J. Yan, J. Knolle, C. A. Bridges, M. B. Stone, M. D. Lumsden, D. G. Mandrus, D. A. Tennant, R. Moessner, and S. E. Nagler, *Science* **356**, 1055 (2017).
- [25] X. Y. Li, D. Reig-i-Plessis, P.-F. Liu, S. Wu, B.-T. Wang, A. M. Hallas, M. B. Stone, C. Broholm, and M. C. Aronson, *Phys. Rev. B* **104**, 10.1103/PhysRevB.104.134305 (2021).
- [26] Y. Goryunov, V. Fritsch, H. v Löhneysen, and A. Nateprov, *Journal of Physics: Conference Series* **391**, 012015 (2012).
- [27] Y. Goryunov and A. Nateprov, Spin and Valence Fluctuation in Eu Compounds with CaAl₂Si₂-Structure, in *Proceedings of the International Conference on Strongly Correlated Electron Systems (SCES2013)*.
- [28] E. Dengler, J. Deisenhofer, H.-A. Krug von Nidda, S. Khim, J. S. Kim, K. H. Kim, F. Casper, C. Felser, and A. Loidl, *Phys. Rev. B* **81**, 024406 (2010).
- [29] F. A. Garcia, A. Leithe-Jasper, W. Schnelle, M. Nicklas, H. Rosner, and J. Sichelschmidt, *New Journal of Physics* **14**, 063005 (2012).
- [30] M. Hemmida, H.-A. Krug von Nidda, A. Günther, A. Loidl, A. Leithe-Jasper, W. Schnelle, H. Rosner, and J. Sichelschmidt, *Phys. Rev. B* **90**, 205105 (2014).
- [31] H.-A. Krug von Nidda, S. Kraus, S. Schaile, E. Dengler, N. Pascher, M. Hemmida, M. J. Eom, J. S. Kim, H. S. Jeevan, P. Gegenwart, J. Deisenhofer, and A. Loidl, *Phys. Rev. B* **86**, 094411 (2012).
- [32] R. Rühl and W. Jeitschko, *Mater. Res. Bull.* **14**, 513 (1979).
- [33] D. Rauch, M. Kraken, F. J. Litterst, S. Süllow, H. Luetkens, M. Brando, T. Förster, J. Sichelschmidt, A. Neubauer, C. Pfeleiderer, W. J. Duncan, and F. M. Grosche, *Phys. Rev. B* **91**, 174404 (2015).
- [34] T. Gruner, J. Wykhoff, J. Sichelschmidt, C. Krellner, C. Geibel, and F. Steglich, *Journal of Physics: Condensed Matter* **22**, 135602 (2010).
- [35] N. Brookes, F. Yakhou-Harris, K. Kummer, A. Fondacaro, J. Cezar, D. Betto, E. Velez-Fort, A. Amorese, G. Ghiringhelli, L. Braicovich, R. Barrett, G. Berruyer, F. Cianciosi, L. Eybert, P. Marion, P. van der Linden, and L. Zhang, *Nuclear Instruments and Methods in Physics Research Section A: Accelerators, Spectrometers, Detectors and Associated Equipment* **903**, 175 (2018).
- [36] K. Kummer, A. Fondacaro, E. Jimenez, E. Velez-Fort, A. Amorese, M. Aspbury, F. Yakhou-Harris, P. van der Linden, and N. B. Brookes, *Journal of Synchrotron Radiation* **23**, 464 (2016).
- [37] J. Sichelschmidt, K. Kliemt, M. Hofmann-Kliemt, and C. Krellner, *Phys. Rev. B* **97**, 214424 (2018).
- [38] R. Kubo and K. Tomita, *Journal of the Physical Society of Japan* **9**, 888 (1954).
- [39] D. L. Huber, G. Alejandro, A. Caneiro, M. T. Causa, F. Prado, M. Tovar, and S. B. Oseroff, *Phys. Rev. B* **60**, 12155 (1999).
- [40] H. Benner and J. P. Boucher, Spin Dynamics in the Paramagnetic Regime: NMR and EPR in Two-Dimensional Magnets, in *Magnetic Properties of Layered Transition Metal Compounds*, edited by L. J. de Jongh (Springer Netherlands, Dordrecht, 1990) pp. 323–378.
- [41] S. Krebber and et al., Supplemental Information (2025).
- [42] A. Weiss, *Berichte der Bunsengesellschaft für physikalische Chemie* **81**, 779 (1977).
- [43] N. S. Sangeetha, S. Pakhira, Q.-P. Ding, L. Krause, H.-C. Lee, V. Smetana, A.-V. Mudring, B. B. Iversen, Y. Furukawa, and D. C. Johnston, *Proceedings of the National Academy of Sciences* **118**, e2108724118 (2021).
- [44] E. M. Brüning, C. Krellner, M. Baenitz, A. Jesche, F. Steglich, and C. Geibel, *Phys. Rev. Lett.* **101**, 117206 (2008).
- [45] R. Sarkar, P. Khuntia, C. Krellner, C. Geibel, F. Steglich, and M. Baenitz, *Phys. Rev. B* **85**, 140409 (2012).
- [46] M. Güttler, A. Generalov, M. M. Otrokov, K. Kummer, K. Kliemt, A. Fedorov, A. Chikina, S. Danzenbächer, S. Schulz, E. V. Chulkov, Y. M. Koroteev, N. Carocanales, M. Shi, M. Radovic, C. Geibel, C. Laubschat, P. Dudin, T. K. Kim, M. Hoesch, C. Krellner, and D. V. Vyalikh, *Sci. Rep.* **6**, 24254 (2016).
- [47] A. Chikina, M. Höpner, S. Seiro, K. Kummer, S. Danzenbächer, S. Patil, A. Generalov, M. Güttler, Y. Kucherenko, E. V. Chulkov, Y. M. Koroteev, K. Koepernik, C. Geibel, M. Shi, M. Radovic, C. Laubschat, and D. V. Vyalikh, *Nature Communications* **5**, 3171 (2014).
- [48] K. Kliemt, M. Bolte, and C. Krellner, *Journal of Physics: Condensed Matter* **30**, 385801 (2018).

VII. SUPPLEMENTAL MATERIAL

A. Heat capacity

Fig. S1 shows the field-dependent heat capacity of EuMn_2P_2 at the T_3 transition. At zero field, a peak appears at 18 K which then shifts to lower temperatures when a field is applied along the c direction. The transition comes from the antiferromagnetic ordering of the Eu^{2+} spins. Fig. S2 shows the zero-field heat capacity of EuMn_2P_2 between 52 K and 200 K. No further transitions are observed in this temperature range.

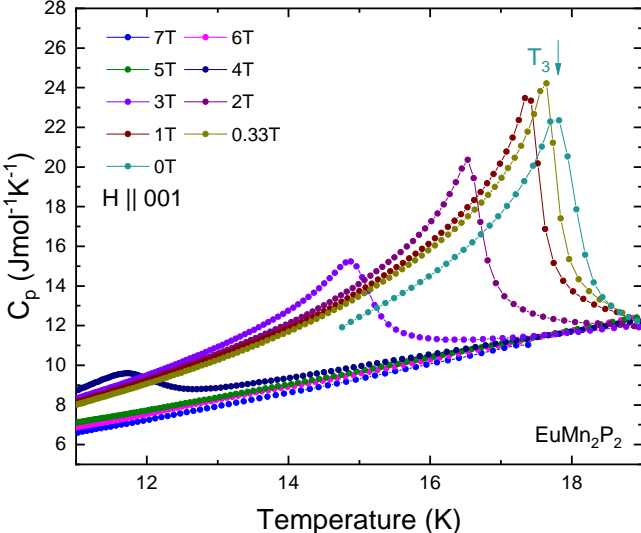


FIG. S1. Heat capacity of EuMn_2P_2 measured in different magnetic fields $H \parallel 001$ below 19 K as a function of temperature. The magnetic transition at T_3 is assigned to the AFM ordering of Eu^{2+} and shifts to lower temperatures with increasing field.

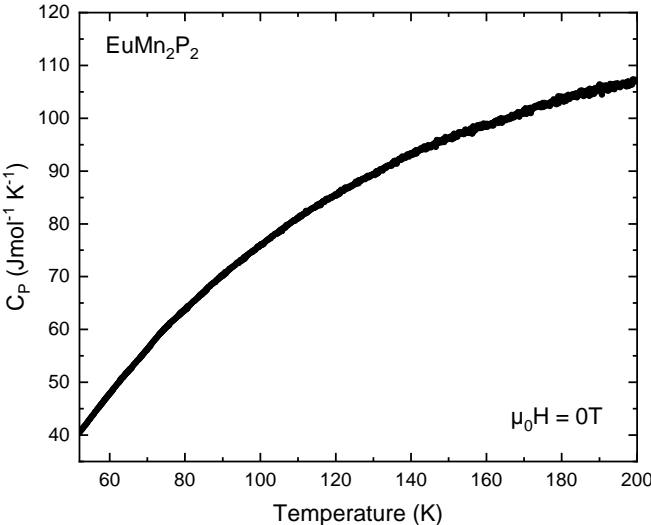


FIG. S2. The zero-field heat capacity of EuMn_2P_2 as a function of temperature between 52 K and 200 K.

B. Magnetic susceptibility and inverse susceptibility

The magnetic susceptibility as a function of temperature for the in-plane- and out-of-plane direction is shown in Fig. S3. Both directions show a peak at $T_3 = 18$ K. Upon increasing the magnetic field, the peak shifts to lower temperatures for both directions, which is comparable with the heat capacity data shown in Fig. S1. The drop at 3.7 K occurs due to Sn inclusions inside the sample, which become superconducting at low fields.

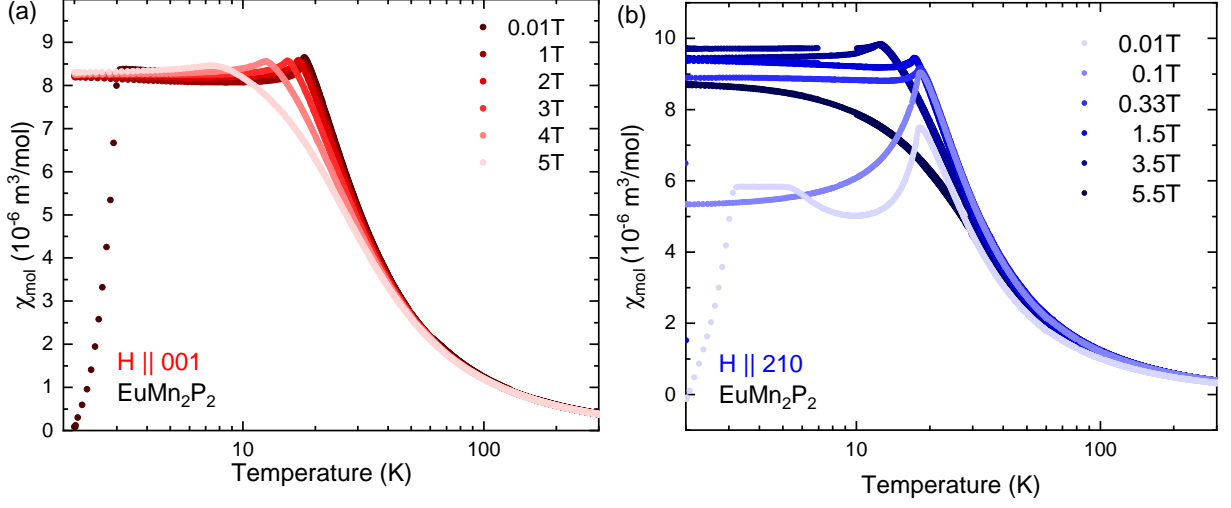


FIG. S3. $\chi_{\text{mol}}(T)$ (a) $H \parallel 001$ and (b) $H \parallel 210$: The Eu transition at T_3 shifts to lower temperatures with increasing field.

The inverse magnetic susceptibility at $\mu_0 H = 1$ T is depicted in Fig. S4 for two field directions. From a Curie-Weiss fit at high temperatures between 150 K and 290 K, the effective moments $\mu_{\text{eff}} = 8.4 \mu_B$ were calculated for field applied along the out-of-plane and in-plane directions.

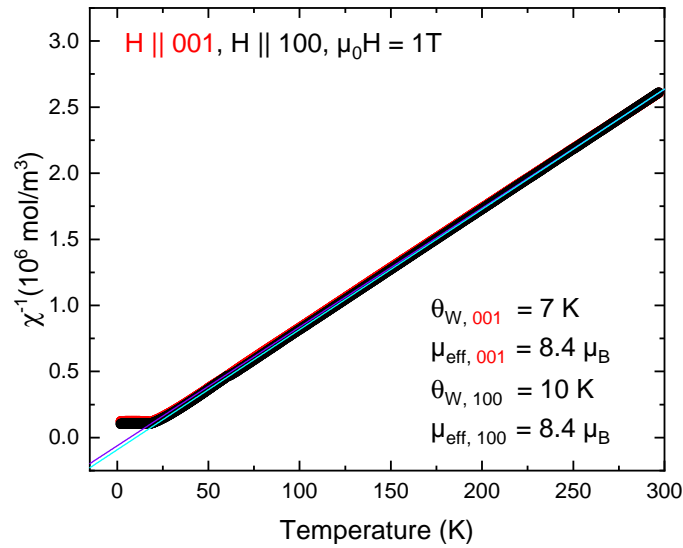


FIG. S4. Inverse magnetic susceptibility $\chi(T)^{-1}$ for $H \parallel 001$ and $H \parallel 100$. The data are fitted using the Curie-Weiss law.

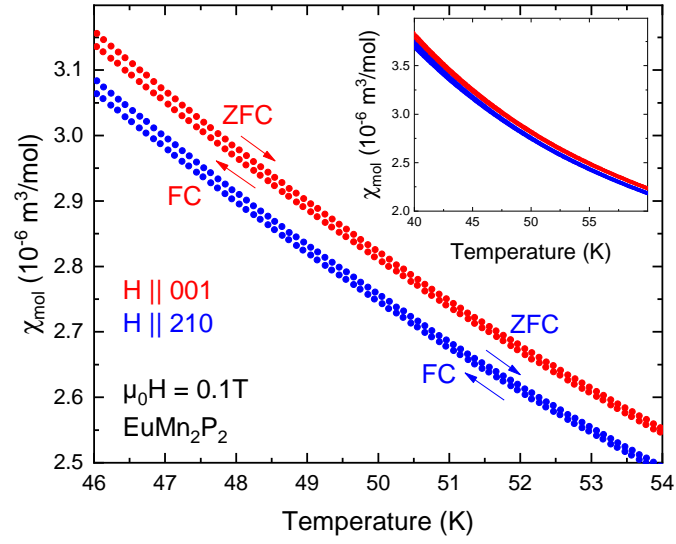


FIG. S5. Comparison of $\chi_{\text{mol}}(T)$ with $H \parallel 001$ (red) and $H \parallel 210$ (blue) close to 50 K measured in FC and ZFC mode.

In Fig. S5, susceptibility data recorded in zero-field cooled and field-cooled mode close to the transitions at $T_{1,2}$ are depicted. While the transition, attributed to magnetic order of Mn is visible in HC, there is no clear feature in $\chi(T)$. If at all, a slight difference between ZFC and FC curve is visible below ≈ 50 K.

C. Field dependence of the moment

Fig. S6(a) shows the moment versus field of EuMn_2P_2 for field along two distinct in-plane directions, [100] and [210], and the out-of-plane direction [001]. At 4 K, the saturated moment reaches $\approx 7\mu_B$. The critical fields are $\mu_0 H_c^{100} = 4.7$ T, and $\mu_0 H_c^{001} = 5.5$ T. This is in contrast to a recent report [20] where $\mu_0 H_c^{001} \approx 4$ T was found.

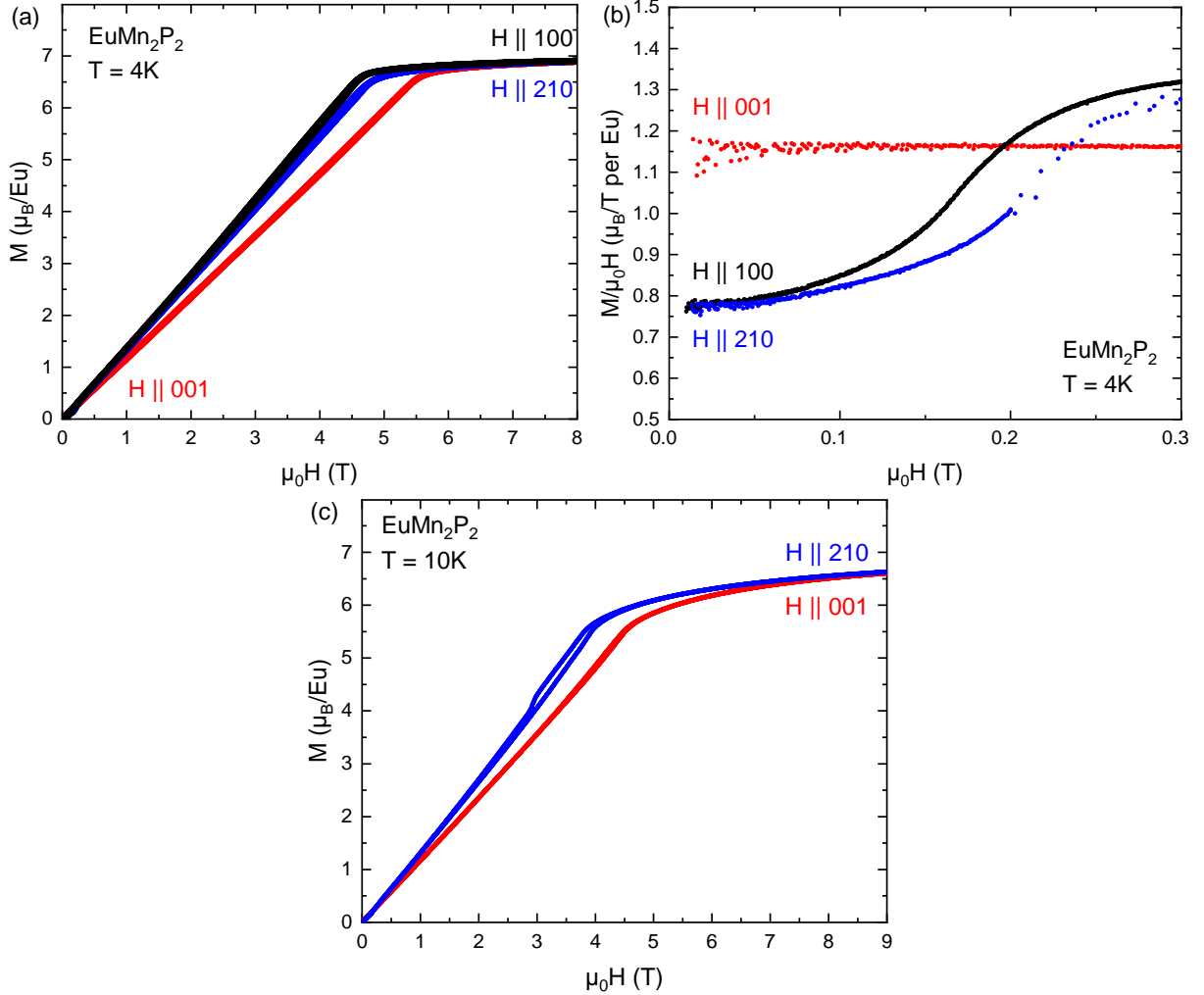


FIG. S6. Comparison of in-plane [100], [210], and out-of-plane [001] direction (a) Magnetic moment $M(H)$ at 4 K. (b) The low-field magnetic susceptibility $M/H(H)$ versus field at 4 K reveals the in-plane/out-of-plane anisotropy as well as a weak in-plane anisotropy. (c) Magnetic moment $M(H)$ at 10 K.

From Fig. S6(b) it is apparent that EuMn_2P_2 shows a very low anisotropy between the in-plane [100] and [210] directions, and the $M/\mu_0 H$ data with field aligned along the [001] direction is almost constant for low fields. When applying the field along the [100] direction, the slope starts changing at a field of ≈ 0.1 T which is slightly lower than the field of ≈ 0.15 T where the slope change occurs in case of field along the [210] direction. The constant value for the [001] directions suggest that the magnetic Eu moments are aligned predominantly in the $a - a$ plane, while the particular response for in-plane fields indicates that in the system with the six AFM domains, the magnetic moments are aligned close to the [100] and symmetric equivalent directions. The data clearly show that at 4 K, the alignment of the Eu spins is not changed by applying a field up to $\mu_0 H \approx 0.05$ T. This is in contrast to the related EuZn_2P_2 [7] and EuCd_2P_2 [6] compounds, where the Eu spin arrangement and domain distribution can be changed using much lower fields. At 10 K, a stronger hysteresis between 2 and 4 T is found for field along the in-plane direction, as shown in Fig. S6(c). This result is in contrast to the data presented in Ref. [20] where the occurrence of a hysteresis in the same field range was observed for $H \parallel 001$. Fig. S7(a,b) show the comparison of $M(H)$ at different temperatures with field applied along [210] and [001]. We furthermore recorded $M(H)$ data close to the $T_{1,2}$ transitions, Fig. S8 and

found no significant change of slope which is consistent with a very weak magnetic contribution from Mn.

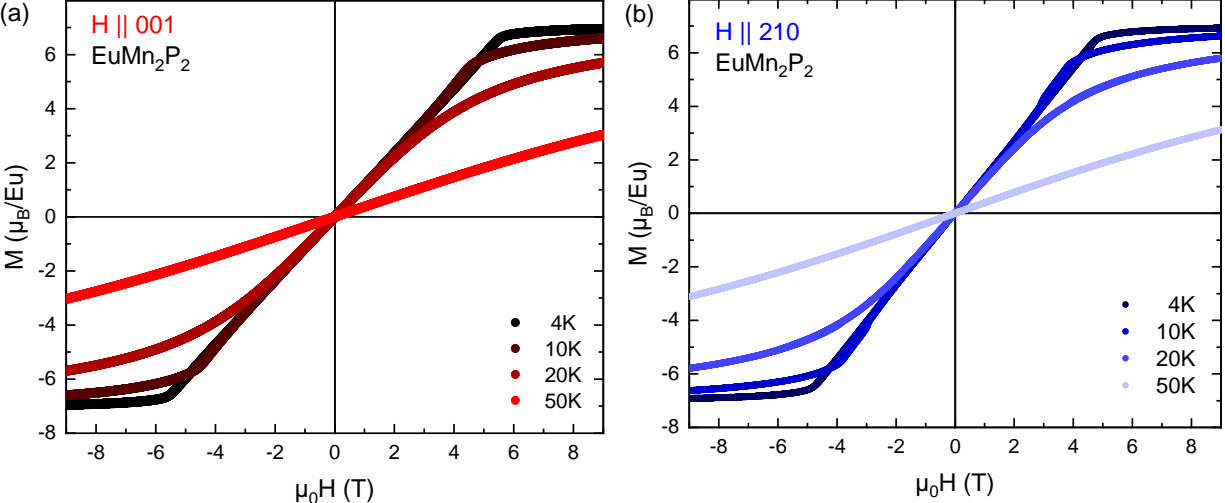


FIG. S7. The moment versus field $M(H)$ for (a) $H \parallel 001$ and (b) $H \parallel 210$ is dominated by the strong magnetism of Eu.

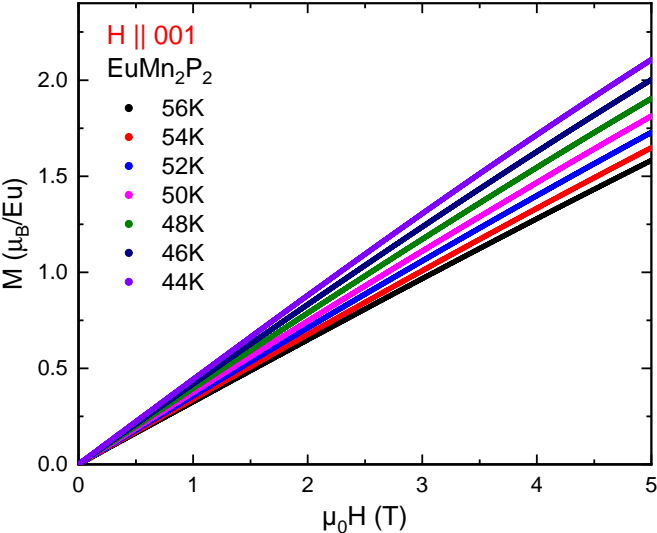


FIG. S8. $M(H)$ at high T close to the putative Mn transition.

D. Resistivity

Fig. S9 shows the temperature dependent resistivity for two different EuMn_2P_2 single crystals, which exhibits a certain sample dependence. At room temperature, both samples are well conducting and upon cooling become increasingly insulating. The resistivity of both crystals shows a broad hump at around ≈ 150 K, however the slope slightly deviates for both samples.

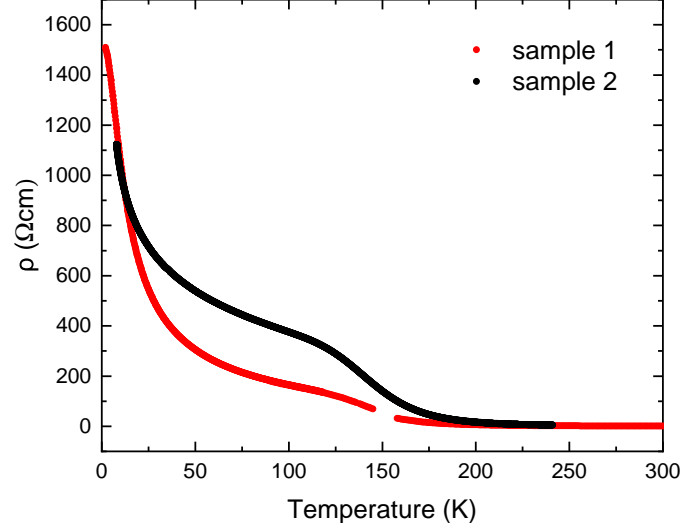


FIG. S9. Temperature dependence of the resistivity ρ at $\mu_0 H = 0$ T with the current in the $a - a$ plane for two different single crystals.

E. NMR

Line width FWHF (full width at half maximum) plotted as function of temperature in Fig. S10. It is clearly recognizable that the line width increases monotonically from room temperature to lower temperatures and then shows a significantly stronger increase below ≈ 100 K. We suspect that this has to do with the onset of critical fluctuations in preparation for the Mn-based order.

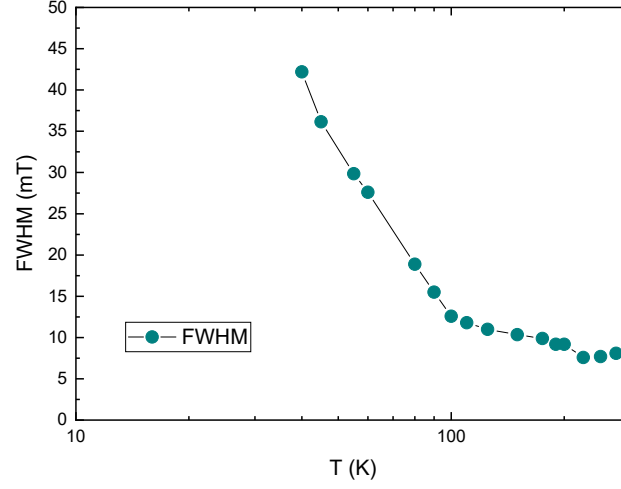


FIG. S10. Full width half maximum (FWHM) of the ^{31}P NMR line as a function of temperature.